PCCP

ROYAL SOCIETY OF CHEMISTRY

PAPER

View Article Online
View Journal | View Issue

Check for updates

Cite this: *Phys. Chem. Chem. Phys.*, 2022, **24**, 29693

First-principles study on bilayer SnP_3 as a promising thermoelectric material†

Hongyue Song,[a] Xuehua Zhang,[a] Peiling Yuan,[a] Wencheng Hu[a] and Zhibin Gao *[b]

Received 7th September 2022,
Accepted 14th November 2022

DOI: 10.1039/d2cp04167g

rsc.li/pccp

The bilayer SnP_3 is recently predicted to exfoliate from its bulk phase, and motivated by the transition of the metal-to-semiconductor when the bulk SnP_3 is converted to the bilayer, we study the thermoelectric performance of the bilayer SnP_3 using first-principles combined with Boltzmann transport theory and deformation potential theory. The results indicate that the bilayer SnP_3 is an indirect band gap semiconductor and possesses high carrier mobility. The high carrier mobility results in a large Seebeck coefficient observed in both n- and p-doped bilayer SnP_3, which is helpful for acquiring a high figure of merit (*ZT*). Moreover, by analyzing the phonon spectrum, relaxation time, and joint density of states, we found that strong phonon scattering makes the phonon thermal conductivity extremely low (~0.8 W m^{-1} K^{-1} at room temperature). Together with a high power factor and a low phonon thermal conductivity, the maximum *ZT* value can reach up to 3.8 for p-type doping at a reasonable carrier concentration, which is not only superior to that of the monolayer SnP_3, but also that of the excellent thermoelectric material SnSe. Our results shed light on the fact that bilayer SnP_3 is a promising thermoelectric material with a better performance than its monolayer phase.

1 Introduction

Thermoelectric (TE) materials have attracted more and more attention due to their ability to directly and reversibly convert waste heat and electricity. The conversion efficiency of a TE material is usually defined as the dimensionless figure of merit ZT,[1] $ZT = S^2\sigma T/\kappa$, where S, σ, T, and κ represent the Seebeck coefficient, electrical conductivity, absolute temperature, and thermal conductivity composed of thermal conductivities of an electron (κ_e) and a phonon (κ_{ph}), respectively. Here, the power factor $S^2\sigma$ is used to balance the properties of the electron. A potential high-performance TE material should have a high ZT value, that is, normally greater than 1 for commercial use. Unfortunately, because of the contradictory relationship between S and σ, together with the Wiedemann–Franz law: $\kappa_e = L\sigma T$ (L is the Lorenz number and for free electrons, $L = 2.45 \times 10^{-8}$ W Ω K^{-2}),[2,3] it is complex to enhance the TE conversion efficiency.[4] Band structure engineering[5] and optimal doping,[6] for instance, are usually used to optimize the power factor. However, κ_{ph} is a relatively independent factor to improve the ZT value,[7–9] and searching materials with low κ_{ph} is of great significance in the TE field.

For example, the famous layered TE material SnSe reported by Zhao *et al.*[10] has an exceptionally low κ_{ph} (0.23 ± 0.03 W m^{-1} K^{-1}) and an unprecedented ZT of ~2.6 at 923 K. Zhao *et al.*[10] attributed the low κ_{ph} in SnSe to the strong anharmonic and anisotropic bonding between layers. The other similar layered structures of bismuth oxychalcogenides including BiCuOX, Bi_2O_2X, and Bi_2OX_2 (X = S, Se, and Te) also possess extremely low κ_{ph}, namely lower than 2 W m^{-1} K^{-1} at 300 K, and show a superior performance among thermoelectric materials.[11–13] Furthermore, much work has been reported to attribute their low κ_{ph} to the anharmonicity of the interlayer coupling resulting from the chemical bonding between Bi and chalcogen atoms.[13–15] In fact, for layered structures, the interlayer coupling provides an additional degree of freedom and thus can be used to tune the properties of materials, in particular for κ_{ph}. Recently, Pei *et al.*[16] have highlighted using stacking order, electric field, intercalation, and pressure of layered materials to control the interlayer coupling, thereby improving their physical properties. Besides, the strategies such as defect engineering,[17] lone-pair electrons,[18] and nanostructuring[19] are also being used to enhance phonon scattering and thus achieving low phonon thermal conductivity.

Recently, novel two-dimensional (2D) SnP_3 materials including their monolayer and bilayer phases have been theoretically predicted to be extracted from their bulk counterpart using a mechanical exfoliation method with thermal stablity.[20–22] The calculated cleavage energies reported by Ghosh *et al.*[20] for

[a] College of Science, Zhengzhou Key Laboratory of Low-dimensional Quantum Materials and Devices, Zhongyuan University of Technology, Zhengzhou 450007, China
[b] State Key Laboratory for Mechanical Behavior of Materials, Xi'an Jiaotong University, Xi'an 710049, China. E-mail: zhibin.gao@xjtu.edu.cn

† Electronic supplementary information (ESI) available. See DOI: https://doi.org/10.1039/d2cp04167g

monolayer and bilayer SnP_3 are 0.71 and 0.45 J m^{-2}, respectively, which are comparable to that of graphene from the corresponding graphite (0.32 J m^{-2}).[23] Significantly, bulk SnP_3 has been synthesized experimentally long since and shows metallicity.[24] Nevertheless, both the monolayer and bilayer SnP_3 are semiconductors having an indirect band gap.[25–27] Monolayer and bilayer SnP_3 have been reported to possess high carrier mobility and optical absorption coefficient, suggesting their potential for applications in the optoelectronic area, such as anode materials in Na- and Li-ion batteries.[20–22,25] Moreover, similar layered structures to SnP_3, that is, monolayer and bilayer GeP_3 are also reported to have a pronounced light absorption coefficient and remarkably high carrier mobility.[28] Besides, in 2019, Zhu *et al.*[29] reported theoretically that the monolayer SnP_3 is an excellent p-type thermoelectric material, namely its ZT can reach 3.46 for optimal hole doping at 500 K, which is comparable to that of the well-known TE material SnSe ($\sim$2.6 at 923 K) mentioned above.[10]

Furthermore, Zhu *et al.*[29] also attribute the high ZT value of the monolayer SnP_3 to its low phonon thermal conductivity ($\sim$4.97 Wm^{-1} K^{-1} at 300 K) and high Seebeck coefficient ($\sim$900 μV K^{-1} at 300 K). Based on the electronic band structure engineering and the TE transport property tuning,[30] Wei *et al.*[31] also reported the strain modulated thermoelectric performance of the monolayer SnP_3, and the results show that although κ_{ph} increases, a considerable ZT of 2.01 at 700 K is also obtained for the 6% strained case.

As far as we know, although the thermoelectric transport properties of the monolayer SnP_3 are widely studied, the electronic and the phonon transport properties of bilayer SnP_3 are still poorly understood. Note that the bilayer SnP_3 can be exfoliated from its bulk structure with dynamical stability, offering a new route for interlayer coupling compared with its monolayer phase. Since interlayer coupling plays an important role in the properties of electrons and phonons, we will perform a systematic investigation on the thermoelectric performance of the bilayer SnP_3 using first-principles theory accompanied by Boltzmann transport theory and deformation potential theory in this work. Our results indicate that the bilayer SnP_3 is a semiconductor with an indirect band gap ($\sim$0.9 eV), and it also possesses high carrier mobility. The flat electronic band structure and several sharp peaks in the electronic density of states (DOSs) near the Fermi energy lead to perfect thermoelectric properties. Furthermore, we found that its room-temperature phonon thermal conductivity is below 1 W m^{-1} K^{-1}, resulting from the strong three-phonon scattering. Owing to the high power factor and the extremely low phonon thermal conductivity, we surprisingly discovered that a maximum ZT value of 3.8 can be obtained for moderate p-type doping at 300 K. This value is higher than that of the monolayer SnP_3.[29] Our results indicate that the TE performance of the bilayer SnP_3 can be improved compared to the monolayer SnP_3, and the bilayer SnP_3 is an excellent TE material.

2 Computational methods

First-principle calculations are carried out based on the framework of density functional theory (DFT) using the Vienna *ab initio* Simulation Package (VASP)[32,33] code. The generalized gradient approximation (GGA) in the form of the Perdew, Burke, and Ernzerhof (PBE)[34] is adopted. For the structural relaxation, the plane wave energy cutoff is picked to be 500 eV, and a 15 × 15 × 1 Monkhorst–Pack k point mesh is used. The energy and the residual force on the atom are set to be 10^{-4} eV and 0.01 eV Å^{-1}, respectively, which can ensure the convergence of the structure relaxation. Moreover, the vacuum space between layers is set to 15 Å along the z-axis to avoid interlayer interactions. Considering that the PBE approach underestimates the electronic band gap of materials, we adopt the Heyd–Scuseria–Ernzerhof (HSE06)[35] functional to obtain a more accurate electronic band gap of the bilayer SnP_3. According to the band structure obtained by the DFT calculations, we adopt the semiclassical Boltzmann theory within the rigid band method[36] and constant relaxation time approximation as implemented within the BoltzTraP code[37] to calculate the electrical transport coefficients such as S and σ/τ except for the carrier relaxation time. In general, the carrier relaxation time τ is related to many factors such as the temperature, lattice structure and doping content.[38] In our work, we adopt the deformation potential theory based on the effective mass approximation to calculate τ.[39] Here, the limitation of the method is that it only considers the dominated scattering contributed by the coupling between free carriers and longitudinal acoustic phonons. Nevertheless, the method has been proven to be valid to predict the mobility of two-dimensional materials, and the results are reliable.[40–42] Here, based on the Wiedemann–Franz law, $\kappa_e = L\sigma T$ where L is the Lorenz number and we use it as 2.45 × 10^{-8} W Ω K^{-2} in our work,[2,3] and the electrical thermal conductivity κ_e can be acquired. In order to obtain accurate transport coefficients, a dense 45 × 45 × 1 k-point mesh is used in the Brillouin zone (BZ). The phonon transport properties are obtained by the Boltzmann transport equation as realized in phonopy[43] and phono3py[44] codes. Together with the VASP, the second- and the third-order interaction force constants (IFCs) are calculated by a finite-difference method using 3 × 3 × 1 and 2 × 2 × 1 supercells, respectively, and with a 2 × 2 × 1 mesh k-points because of the computing resource. Besides, the energy convergence is set to 10^{-8} eV. Here, the carefully tested k-points of 21 × 21 × 1 in the BZ are used to calculate the phonon thermal conductivity.

3 Results and discussion

The crystal structure of SnP_3 in the bulk phase is a widely known layered material and belongs to the trigonal space group $R\bar{3}m$ (166).[45] From the side and top views, the structures of each layer combined with P and Sn atoms are analogous to those of blue phosphorene with a puckered type and graphene with a honeycomb type, respectively. Owing to the weak van der Waals interactions between the layers, it has been theoretically reported that the monolayer and bilayer SnP_3 can be relatively easy to exfoliate from the bulk phase based on DFT calculations.[20–22] The calculated cleavage energies reported by

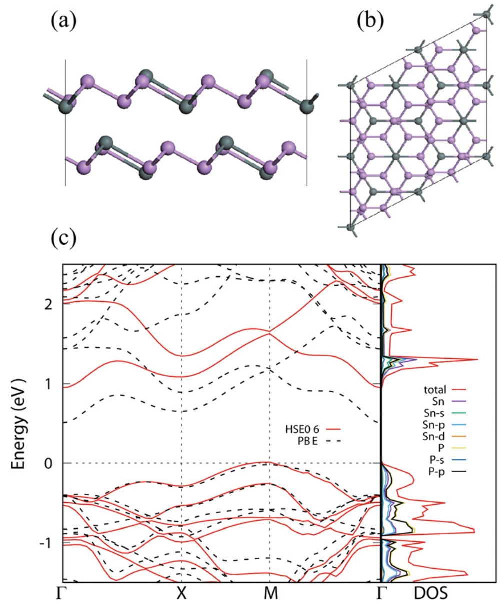

Fig. 1 (a and b) Structures of the side view and top view of the bilayer SnP_3 (purple: P atoms and gray: Sn atoms). (c) Electronic band structures using the potentials of PBE and HSE06, and the total and partial DOSs of the bilayer SnP_3. The high symmetry k points are Γ (0, 0, 0), X (0.5, 0, 0) and M (0.33, 0.33, 0).

Ghosh *et al.*[20] for monolayer and bilayer SnP_3 are 0.71 and 0.45 J m^{-2}, respectively, which can be comparable to that of graphene from the corresponding graphite (0.32 J m^{-2}).[23] Afterwards, Sun *et al.*[21] and Feng *et al.*[22] also reported the theoretical cleavage energies of these two novel 2D materials and predicted that monolayer and bilayer SnP_3 can be fabricated using a stripping method. The structure of the bilayer SnP_3 is shown in Fig. 1(a and b). The optimized lattice parameter is $a = b = 7.49$ Å, which is consistent with the results reported by Ghost *et al.*[20] Meanwhile, the value is a little larger than those of the in-plane of bulk SnP_3 (7.38 Å)[46] and monolayer SnP_3 (7.37 Å).[29] More details about lattice parameters and atomic positions of the bilayer SnP_3 are given in section A in the ESI.†

In Fig. 1(c), we present the electronic band structures of the bilayer SnP_3 in PBE and HSE06 hybrid functional potentials and the total and partial electronic density of states (DOSs). The results show that the bilayer SnP_3 is a semiconductor with a valence band maximum (VBM) and a conduction band minimum (CBM) located at the M and Γ points, respectively. According to the method of the PBE potential, the calculated band gap is 0.5 eV, which is always underestimated compared to the experimental value. Then, the more accurate band gap obtained by the HSE06 functional is 0.9 eV. Thus, the next calculation of the electronic transport properties is all based on the HSE06 approach. It is worth mentioning that the two-fold degeneracy appears in the conduction band at the M point, which is useful for band engineering to improve the ZT value. For example, Wei *et al.*[31] have reported the strain-tuned band structure and the thermoelectric properties of the monolayer SnP_3, and it possesses a promising ZT value at a 6% strained case.

Besides, Fig. 1(c) also shows that the valence band is flatter than the conduction band suggesting the higher Seebeck coefficients for the hole-doped bilayer SnP_3. From the DOS plots, we can see that the top of the valence band is contributed mainly by the P atoms, while the bottom of the conduction band is dominated by the Sn atoms. Further analysis shows that this contribution mainly originates from the p orbitals for both cases.

According to the electronic band structure, the electronic transport coefficients including the Seebeck coefficient, electrical conductivity, and power factor are obtained by using the Boltzmann transport theory (BTE) within the method of constant relaxation approximation (CRTA). The results as a function of the carrier concentration at 300, 500, and 700 K are shown in Fig. 2. We can see that the bilayer SnP_3 exhibits a high Seebeck coefficient for both p- and n-type doping, and the value of S of hole doping is slightly higher than that of electron doping, which is ascribed to the flatter valence band than the conduction band displayed in Fig. 1, and, also leading to a higher effective mass of holes than that of the electrons presented in Table 1. For instance, the maximum Seebeck coefficients of 620 and 510 μV K^{-1} at 300 K are obtained for the p- and n-doped bilayer SnP_3, respectively, which facilitated achieving high ZT values.

Moreover, the temperature-dependent Seebeck coefficient shows normal characteristics, that is, with the increasing temperature (both holes and electrons), the Seebeck coefficient gradually increases. Based on the BTE, the results of the electrical conductivity (σ/τ) are shown in Fig. 2(c) and (d). Therefore, there is an issue that should be pointed out, namely, we need the carrier relaxation time which is hard to acquire with high precision. Here, we use the approach of the

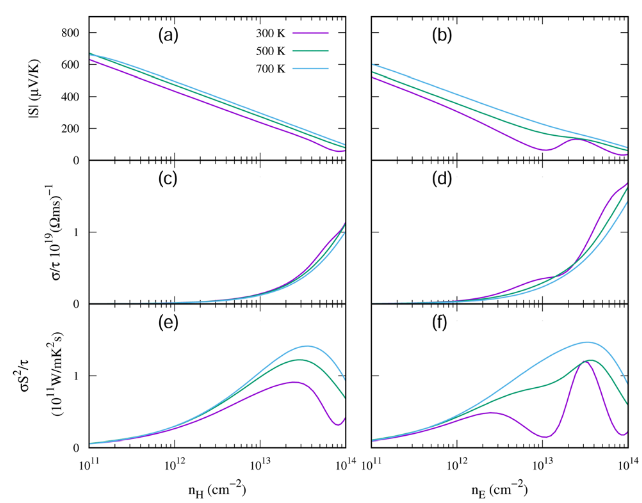

Fig. 2 Electronic transport coefficients including S (a and b), σ/τ (c and d), and $S^2\sigma/\tau$ (e and f) as a function of the carrier concentration at 300, 500 and 700 K. The left panel is for p-type doping and the right is for n-type doping. The horizontal ordinate is calculated by the number of doped carriers divided by the bottom area of the crystal structure.

Table 1 Effective mass m^*, elastic modulus C_{2D}, deformation potential constant E_l, carrier mobility μ, and relaxation time τ for electrons and holes of the bilayer SnP_3 at 300 K

Carriers	$m^*_{\Gamma-X}(m_e)$	$m^*_{X-K}(m_e)$	C_{2D} (J m^{-2})	E_l (eV)	μ (cm^2 V^{-1} s^{-1})	τ (10^{-13} s)
e	0.23	0.26	98.77	−4.48	1833	2.4
h	−0.66	−0.68	98.77	1.96	1477	4.6

deformation potential theory to evaluate τ, and the detailed calculation process will be discussed in the next section.

Fig. 2(c) and (d) indicate that σ/τ shows an opposite tendency to temperature and the tendency of carrier concentration is found to be that of the Seebeck coefficient. Furthermore, owing to the smaller effective mass for electrons than the hole, a larger σ/τ of n-type doping is obtained than p-type doping for the same carrier concentration. Based on the calculated Seebeck coefficient and the electrical conductivity, the results of the power factor ($S^2\sigma/\tau$) are shown in Fig. 2(e) and (f). Looking at the temperature dependence, we found that, at 300 K, the $S^2\sigma/\tau$ of electron doping is slightly higher than that of hole doping, indicating that, to improve the thermoelectric performance in the bilayer SnP_3, the n-type doping is more superior compared with p-type doping, which is contrary to the case of the monolayer SnP_3.[31] However, at 500 and 700 K temperatures, both p- and n-type $S^2\sigma/\tau$ show almost the same value for the same carrier concentration. Besides, $S^2\sigma/\tau$ also shows the same temperature dependence with the Seebeck coefficient, rather than that of σ/τ, which is similar to the previous studies about other materials.[47–49] In the end, the temperature dependence of the chemical potential is considered by the formula: $dF = -pdV - SdT + \mu dN$, where F, p, V, S, T, μ and N are the Helmholtz free energy, pressure, volume, entropy, temperature, chemical potential and number of particles, respectively. Then, we can make the more useful definitions: $\mu = \left(\frac{\partial F}{\partial N}\right)_{V,T}$. And we also provide the electronic transport coefficients as a function of the μ at 300, 500 and 700 K in Section B in the ESI.†

In order to obtain the carrier relaxation time τ, the deformation potential theory which has been proved feasible in many two-dimensional materials is adopted.[50] The detailed calculation method is as follows:[51,52]

$$\tau = \frac{\mu m^*}{e} \tag{1}$$

$$\mu = \frac{e\hbar^3 C_{2D}}{k_B T m^* m_d E_l^2} \tag{2}$$

where μ and m^* are the carrier mobility and effective mass, respectively. C_{2D} (see Fig. S2(b), ESI†) named the effective elastic modulus can be calculated by $C_{2D} = \frac{1}{S_0}\frac{\partial^2 E}{\partial(\Delta a/a_0)^2}$ where E, S_0, and $\Delta a/a_0$ are the total energy of the strained cases, the area of the unit cells, and the biaxial strain. E_l (see Fig. S2(a), ESI†) is the deformation potential constant calculated by the slope of the maximum energy at the top of the valence or the minimum value at the bottom of the conduction band as a function of the strained cases. m_d is the average effective mass computed by $m_d = \sqrt{m^*_{\Gamma-X}m^*_{X-K}}$. All the obtained parameters of the bilayer SnP_3 are shown in Table 1. Clearly, the effective masses are nearly equal along the directions of Γ–X and X–K for both electrons and holes. Due to the low effective mass and the deformation potential constant, large carrier mobilities are obtained in the bilayer SnP_3, namely 1833 and 1477 cm^2 V^{-1} s^{-1} for electrons and holes, respectively. Thus, the calculated relaxation times in the bilayer SnP_3 are 0.24 ps for electrons and 0.46 ps for holes, and more computational details are shown in Section C in the ESI.† Although there is no direct experimentally measured τ for the bilayer SnP_3, our calculated τ shows almost the same order as that of other two-dimensional materials.[29,53,54]

With the above discussion of the electronic transport properties of the bilayer SnP_3, the phonon dispersion and phonon thermal conductivity are now briefly discussed. Fig. 3(a) shows the calculated phonon dispersion and the corresponding phonon total and partial DOS. First, there is no imaginary frequency in the phonon dispersion, and this also confirms the dynamical stability of the bilayer SnP_3 construction. Moreover, we can see that the maximum frequency of the acoustic phonon mode is 1.7 THz, which is a sign of the low group velocity resulting in the low phonon thermal conductivity. Similarly, the stronger coupling between the acoustic and the optical phonon modes also predicts the decreased phonon thermal conductivity compared to the monolayer SnP_3.[29] We also note that a phonon gap appears at ∼6 THz separating the spectrum, and the low-frequency part of the spectrum is dominantly contributed by Sn and P atoms, while the high part is mainly by P atoms.

The phonon group velocity has great effects on κ_{ph}, and Fig. 3(b) shows the results of bilayer SnP_3. LA and TA branches at the Γ point are 3.09 and 4.93 km s^{-1}, respectively, and are a little bit larger than those of the monolayer SnP_3.[29] Fig. 4(a) shows the calculated phonon thermal conductivity as a function of the temperature ranging from 100 K to 900 K for bilayer SnP_3. Obviously, the κ_{ph} value decreases with the increasing temperature and follows $1/T$ dependence. Additionally, the κ_{ph} value is 0.8 W m^{-1} K^{-1} at 300 K, which is nearly one-fifth of its monolayer phase (∼4.97 Wm^{-1} K^{-1} marked the black diamond in Fig. 4(a)[29]). Furthermore, the κ_{ph} of the bilayer SnP_3 is almost equal to that of the monolayer InP_3 (∼0.63 W m^{-1} K^{-1} reported

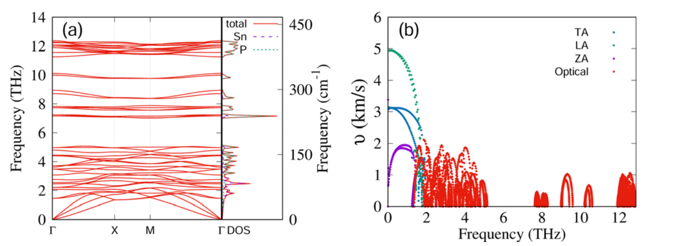

Fig. 3 Phonon dispersion and phonon total and partial DOSs (a) and the phonon group velocity (b) of the bilayer SnP_3.

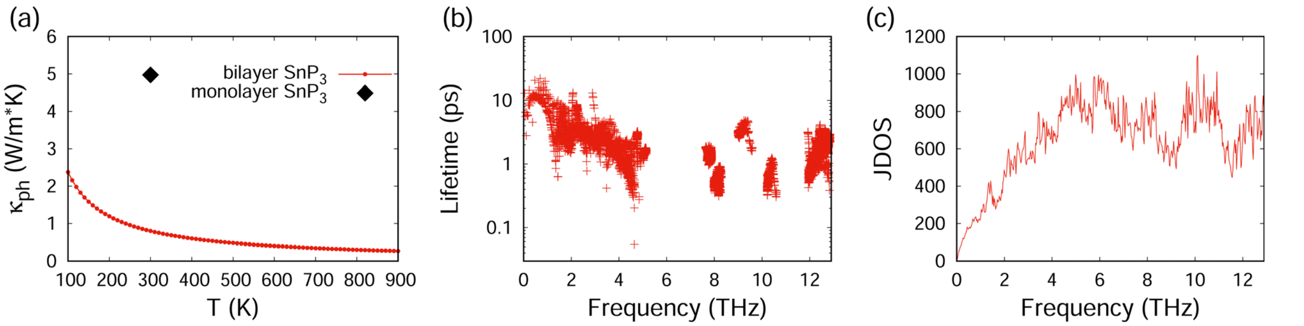

Fig. 4 (a) Phonon thermal conductivity as a function of temperature for the bilayer SnP_3. (b) Phonon relaxation lifetime and (c) JDOS as a function of the frequency for the bilayer SnP_3. The black diamond in (a) marks the κ_{ph} of the monolayer SnP_3 at 300 K reported by Zhu *et al.*[29]

by Ouyang *et al.*[55]) and twice that of the monolayer GeP_3 ($\sim$0.43 W m^{-1} K^{-1} reported by Wang *et al.*[56]), which can be expected to achieve a large *ZT* value. In order to further understand the low κ_{ph}, we calculate the phonon relaxation lifetime and the joint density of states (JDOS) shown in Fig. 4 to analyze the three-phonon scattering.

Fig. 4(b) shows that the phonon relaxation lifetime of the acoustic modes is longer than that of the optical modes, which is consistent with the fact that the acoustic modes usually contribute most of the phonon thermal conductivity. Besides, the shorter phonon relaxation lifetime compared with the monolayer phase[29] signifies a stronger anharmonic phonon scattering process, and thus leading to the low phonon thermal conductivity for bilayer SnP_3. Furthermore, the number of anharmonic phonon scattering named the JDOS is expressed as follows:

$$D(\omega) = \frac{1}{N}\sum_{\lambda_1,\lambda_2}\left[\delta(\omega+\omega_{\lambda_1}-\omega_{\lambda_2})+\delta(\omega-\omega_{\lambda_1}+\omega_{\lambda_2})\right] + \frac{1}{N}\sum_{\lambda_1,\lambda_2}\delta(\omega-\omega_{\lambda_1}-\omega_{\lambda_2}). \quad (3)$$

Here, ω, ω_{λ_1} and ω_{λ_2} are the frequency of the three-phonon scattering. From Fig. 4(c), we found that the large JDOS distributed in the low frequency range grows, while in the high frequency range the JDOS does not almost change. These results tend to increase the phase space for acoustics modes and anharmonic scattering, which results in the low κ_{ph} for bilayer SnP_3.

With the electron and phonon transport coefficients calculated above, the *ZT* value of bilayer SnP_3 can be estimated. The calculated *ZT* values with the change of the carrier concentration at 300, 500, and 700 K are shown in Fig. 5. The results indicate that the *ZT* value for hole doping is obviously higher than that for electron doping, which mainly results from the large power factor caused by the high carrier relaxation time for hole doping. Moreover, the hole doping case needs a higher carrier concentration than electron doping to obtain the maximum *ZT* value. The maximum *ZT* at 300 K is 3.8 for the hole doping bilayer SnP_3 at an appropriate carrier concentration, which is not only higher than some famous thermoelectric materials such as SnSe (2.6),[10] $SnSe_2$ (2.95),[57] black-P (0.22),[58] phosphorene (0.3),[58] and Bi_2Te_3 (1.3),[59] but also can be comparable to its similar layered structures of the monolayer GeP_3 (3.3)[56] and monolayer SnP_3 (2.5)[29] as shown in Fig. 6. In our work, only the scattering between electrons and longitudinal acoustic phonons are considered; in fact, other phonon modes, defects, and grain boundaries can also scatter electrons, leading to reducing the carrier mobility, and thus reducing the *ZT* value accordingly. Therefore, the current theoretical calculation will sometimes underestimate scattering and thus overestimate *ZT*. Furthermore, it should also be pointed out that with the increasing temperature, the *ZT* values are improved for both hole doping and electron doping. In the end, due to the low κ_{ph},

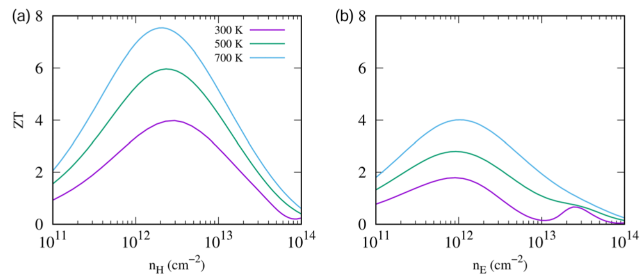

Fig. 5 The calculated *ZT* values of the bilayer SnP_3 as a function of the carrier concentration at different temperatures for (a) p-type doping and (b) n-type doping. The definition of the horizontal ordinate is the same as that shown in Fig. 2.

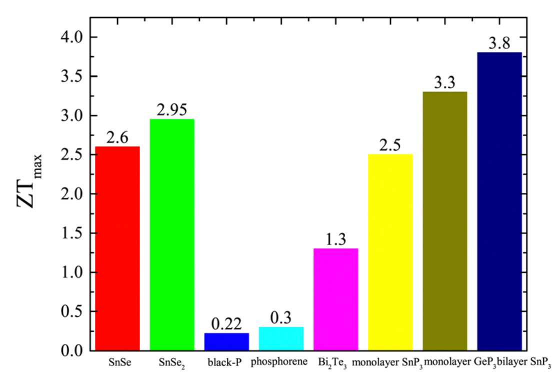

Fig. 6 Compared the *ZT* value of the bilayer SnP_3 with some well-known thermoelectric materials: SnSe,[10] $SnSe_2$,[57] black-P,[58] phosphorene,[58] Bi_2Te_3,[59] monolayer SnP_3,[29] and monolayer GeP_3.[56]

we also calculate the electronic contribution to the figure of merit (ZT_e); here, $ZT_e = S^2\sigma T/\kappa_e$, and the results are presented in Section D in the ESI.† It shows a large difference to the ZT; therefore, the contribution of lattice vibrations to the TE performance cannot be ignored for the SnP_3.

4 Conclusions

In summary, we have studied the thermoelectric transport properties of bilayer SnP_3 using DFT together with Boltzmann transport theory. Our results indicate that it is a semiconductor with an indirect band gap of 0.9 eV calculated using the HSE06 hybrid functional potential. Based on the flat valence and conduction band structures near the Fermi level, high Seebeck coefficients for both n- and p-type doping are observed. Moreover, the bilayer SnP_3 possesses high carrier mobility resulting from the low effective mass and the deformation potential constant, which is beneficial to electrical transport. Owing to the strong scattering phase space between the acoustic and optical phonon modes resulting in a short phonon lifetime, the bilayer SnP_3 exhibits an extremely low phonon thermal conductivity, namely 0.8 W m^{-1} K^{-1} at 300 K, and these results are useful to obtain a high thermoelectric performance. Together with the high power factor and the low phonon thermal conductivity, the maximum ZT value at 300 K can reach 3.8 with an appropriate carrier concentration for hole doping. Here, we should point out that only the dominated scattering mechanism contributed by the coupling between free carriers and longitudinal acoustic phonons is considered in our calculation methods, resulting in the calculated ZT values sometimes overestimated. As a matter of fact, the electron scattering by other phonon modes, defects, grain boundaries, *etc.* cannot be neglected in nanoscale materials, which will suppress the ZT value, resulting in overestimation of the calculated ZT value. A more accurate method to calculate the electronic transport properties is based on the maximally localized Wannier functions which can be calculated by the EPW code.[60] Therefore, our results indicate that the bilayer SnP_3 is a promising thermoelectric material, and we hope that an experimentally high ZT value of the p-doped bilayer SnP_3 can be achieved in the future.

Conflicts of interest

There are no conflicts to declare.

Acknowledgements

Z. G. acknowledges the support of the National Natural Science Foundation of China (No. 12104356), China Postdoctoral Science Foundation (No. 2022M712552), the Opening Project of Shanghai Key Laboratory of Special Artificial Microstructure Materials and Technology (Ammt2022B-1), and the Fundamental Research Funds for the Central Universities. We also acknowledge the support by HPC Platform, Xi'an Jiaotong University.

Notes and references

1 S. M. Pourkiaei, M. H. Ahmadi, M. Sadeghzadeh, S. Moosavi, F. Pourfayaz, L. Chen, M. A. P. Yazdi and R. Kumar, *Energy*, 2019, **186**, 115849.
2 M. Jonson and G. D. Mahan, *Phys. Rev. B*, 1980, **21**, 4223–4229.
3 N. Stojanovic, D. H. S. Maithripala, J. M. Berg and M. Holtz, *Phys. Rev. B*, 2010, **82**, 075418.
4 G. J. Snyder and E. S. Toberer, *Nat. Mater.*, 2008, **7**, 105–114.
5 Y. Pei, X. Shi, A. LaLonde, H. Wang, L. Chen and G. J. Snyder, *Nature*, 2011, **473**, 66–69.
6 J. P. Heremans, V. Jovovic, E. S. Toberer, A. Saramat, K. Kurosaki, A. Charoenphakdee, S. Yamanaka and G. J. Snyder, *Science*, 2008, **321**, 554–557.
7 M. S. Dresselhaus, G. Chen, M. Y. Tang, R. Yang, H. Lee, D. Wang, Z. Ren, J.-P. Fleurial and P. Gogna, *Adv. Mater.*, 2007, **19**, 1043–1053.
8 A. I. Hochbaum, R. Chen, R. D. Delgado, W. Liang, E. C. Garnett, M. Najarian, A. Majumdar and P. Yang, *Nature*, 2008, **451**, 163–167.
9 S. Lee, K. Esfarjani, T. Luo, J. Zhou, Z. Tian and G. Chen, *Nat. Commun.*, 2014, **5**, 1–8.
10 L.-D. Zhao, S.-H. Lo, Y. Zhang, H. Sun, G. Tan, C. Uher, C. Wolverton, V. P. Dravid and M. G. Kanatzidis, *Nature*, 2014, **508**, 373–377.
11 L. Zhao, D. Berardan, Y. Pei, C. Byl, L. Pinsard-Gaudart and N. Dragoe, *Appl. Phys. Lett.*, 2010, **97**, 092118.
12 P. Ruleova, C. Drasar, P. Lostak, C.-P. Li, S. Ballikaya and C. Uher, *Mater. Chem. Phys.*, 2010, **119**, 299–302.
13 H.-Y. Song, X.-J. Ge and J.-T. Lü, *AIP Adv.*, 2020, **10**, 125314.
14 H. S. Ji, A. Togo, M. Kaviany, I. Tanaka and J. H. Shim, *Phys. Rev. B*, 2016, **94**, 115203.
15 H.-Y. Song, X.-J. Ge, M.-Y. Shang, J. Zhang and J.-T. Lü, *Phys. Chem. Chem. Phys.*, 2019, **21**, 18259–18264.
16 S. Pei, Z. Wang and J. Xia, *ACS Nano*, 2022, **16**, 11498–11503.
17 Y. Zheng, T. J. Slade, L. Hu, X. Y. Tan, Y. Luo, Z.-Z. Luo, J. Xu, Q. Yan and M. G. Kanatzidis, *Chem. Soc. Rev.*, 2021, **50**, 9022.
18 M. K. Jana, K. Pal, U. V. Waghmare and K. Biswas, *Angew. Chem.*, 2016, **128**, 7923–7927.
19 J. Ma, O. Delaire, A. May, C. Carlton, M. McGuire, L. VanBebber, D. Abernathy, G. Ehlers, T. Hong, A. Huq, W. Tian, V. Keppens, Y. Shao-Horn and B. Sales, *Nat. Nanotechnol.*, 2013, **8**, 445–451.
20 B. Ghosh, S. Puri, A. Agarwal and S. Bhowmick, *J. Phys. Chem. C*, 2018, **122**, 18185–18191.
21 S. Sun, F. Meng, H. Wang, H. Wang and Y. Ni, *J. Mater. Chem. A*, 2018, **6**, 11890–11897.
22 L.-P. Feng, A. Li, P.-C. Wang and Z.-T. Liu, *J. Phys. Chem. C*, 2018, **122**, 24359–24367.
23 E. Ziambaras, J. Kleis, E. Schröder and P. Hyldgaard, *Phys. Rev. B*, 2007, **76**, 155425.
24 O. Olofsson, U. Aava, A. Haaland, D. Resser, S. Rasmussen and E. Sunde, *Acta Chem. Scand.*, 1970, **24**, 1153–1162.
25 C.-S. Liu, X.-L. Yang, J. Liu and X.-J. Ye, *ACS Appl. Energy Mater.*, 2018, **1**, 3850–3859.
26 J. Du and G. Jiang, *Nanotechnology*, 2020, **31**, 325504.

27 P.-L. Gong, F. Zhang, L.-F. Huang, H. Zhang, L. Li, R.-C. Xiao, B. Deng, H. Pan and X.-Q. Shi, *J. Phys.: Condens. Matter*, 2018, **30**, 475702.
28 Y. Jing, Y. Ma, Y. Li and T. Heine, *Nano Lett.*, 2017, **17**, 1833–1838.
29 X.-L. Zhu, P.-F. Liu, J. Zhang, P. Zhang, W.-X. Zhou, G. Xie and B.-T. Wang, *Nanoscale*, 2019, **11**, 19923–19932.
30 G. Tan, F. Shi, S. Hao, H. Chi, L.-D. Zhao, C. Uher, C. Wolverton, V. P. Dravid and M. G. Kanatzidis, *J. Am. Chem. Soc.*, 2015, **137**, 5100–5112.
31 S. Wei, C. Wang, S. Fan and G. Gao, *J. Appl. Phys.*, 2020, **127**, 155103.
32 G. Kresse and J. Furthmuller, *Comput. Mater. Sci.*, 1996, **6**, 15–50.
33 G. Kresse and J. Furthmüller, *Phys. Rev. B*, 1996, **54**, 11169.
34 J. P. Perdew, K. Burke and M. Ernzerhof, *Phys. Rev. Lett.*, 1996, **77**, 3865.
35 J. Heyd, G. E. Scuseria and M. Ernzerhof, *J. Chem. Phys.*, 2003, **118**, 8207–8215.
36 M.-S. Lee and S. D. Mahanti, *Phys. Rev. B*, 2012, **85**, 165149.
37 G. K. Madsen and D. J. Singh, *Comput. Phys. Commun.*, 2006, **175**, 67–71.
38 L. Bertini and C. Gatti, *J. Chem. Phys.*, 2004, **121**, 8983–8989.
39 J. Bardeen and W. Shockley, *Phys. Rev.*, 1950, **80**, 72.
40 N. Wang, M. Li, H. Xiao, H. Gong, Z. Liu, X. Zu and L. Qiao, *Phys. Chem. Chem. Phys.*, 2019, **21**, 15097–15105.
41 M. Long, L. Tang, D. Wang, Y. Li and Z. Shuai, *ACS Nano*, 2011, **5**, 2593–2600.
42 G. Ding, G. Gao, Z. Huang, W. Zhang and K. Yao, *Nanotechnology*, 2016, **27**, 375703.
43 A. Togo and I. Tanaka, *Scr. Mater.*, 2015, **108**, 1–5.
44 A. Togo, L. Chaput and I. Tanaka, *Phys. Rev. B*, 2015, **91**, 094306.
45 J.-W. Park and C.-M. Park, *Sci. Rep.*, 2016, **6**, 1–8.
46 J. Gullman and O. Olofsson, *J. Solid State Chem.*, 1972, **5**, 441–445.
47 G. Li, G. Ding and G. Gao, *J. Phys.: Condens. Matter*, 2016, **29**, 015001.
48 W. Shi, N. Ge, X. Wang and Z. Wang, *J. Phys. Chem. C*, 2021, **125**, 16413–16419.
49 Z. Gao, G. Liu and J. Ren, *ACS Appl. Mater. Interfaces*, 2018, **10**, 40702–40709.
50 X.-Y. Mi, X. Yu, K.-L. Yao, X. Huang, N. Yang and J.-T. Lü, *Nano Lett.*, 2015, **15**, 5229–5234.
51 Y. Cai, G. Zhang and Y.-W. Zhang, *J. Am. Chem. Soc.*, 2014, **136**, 6269–6275.
52 L.-C. Zhang, G. Qin, W.-Z. Fang, H.-J. Cui, Q.-R. Zheng, Q.-B. Yan and G. Su, *Sci. Rep.*, 2016, **6**, 1–9.
53 G. Ding, C. Wang, G. Gao, K. Yao, C. Dun, C. Feng, D. Li and G. Zhang, *Nanoscale*, 2018, **10**, 7077–7084.
54 C. Wang, G. Gao and S. Lin, *Results Phys.*, 2021, **30**, 104810.
55 T. Ouyang, E. Jiang, C. Tang, J. Li, C. He and J. Zhong, *J. Mater. Chem. A*, 2018, **6**, 21532–21541.
56 C. Wang, Z. Xu, K. Xu and G. Gao, *Molecules*, 2021, **26**, 6376.
57 Y. Ding, B. Xiao, G. Tang and J. Hong, *J. Phys. Chem. C*, 2017, **121**, 225–236.
58 H. Lv, W. Lu, D. Shao and Y. Sun, *arXiv*, 2014, preprint, arXiv:1404.5171, DOI: 10.48550/arXiv.1404.5171.
59 J. Pei, B. Cai, H.-L. Zhuang and J.-F. Li, *Natl. Sci. Rev.*, 2020, **7**, 1856–1858.
60 S. Poncé, E. R. Margine, C. Verdi and F. Giustino, *Comput. Phys. Commun.*, 2016, **209**, 116–133.